Electronic Supplementary Material (ESI) for Lab on a Chip.

Electronic Supplementary Information for

Optical 4D oxygen mapping of microperfused tissue models with tunable in-vivo like 3D oxygen microenvironments

*Milan Finn Wesseler, Mathias Nørbæk Johansen, Aysel Kızıltay, Kim I. Mortensen, and Niels B. Larsen**

Department of Health Technology, DTU Health Tech, Technical University of Denmark, 2800 Kgs. Lyngby, Denmark
E-mail: nibl@dtu.dk

1 Development of the data processing methodology

1.1 Data processing flow

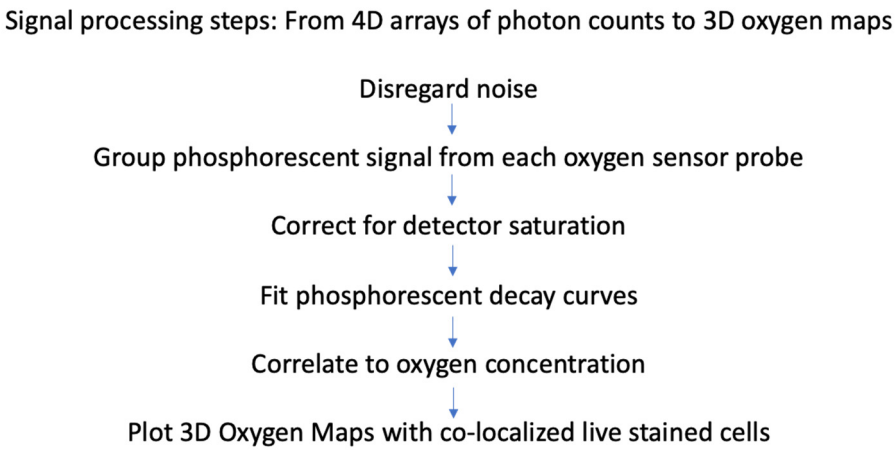

Fig. S1 Signal processing steps to go from 4D arrays of photon counts to 3D visualizations of oxygen sensor probes.

Fig. S1 shows the main signal processing steps needed to go from 4D arrays containing phosphorescent photon counts to 3D visualizations of oxygen sensor probes. First, the 4D arrays of phosphorescent photon counts were summed in their time dimension and all voxels of the resulting 3D matrix with less than 5 photons were disregarded as background noise. This was above the background signal threshold from the microscope without samples and typically decreased the fraction of remaining voxels to <1%. Next, 3D photon intensity maps were transformed into a 3D binary image (1 for >0 photons, 0 otherwise) and objects that consisted of more than 15 voxels with connected faces were identified. Given the size of the oxygen sensor beads (Ø50 µm), objects with less than 15 voxels were considered out of focus beads or background. Some beads in close proximity were grouped into a single object when applying the low noise threshold of 5 photons only. To separate incorrectly grouped beads, voxels in each grouped object with less than 20% of the maximum intensity voxel contained in that same object were deleted. Afterwards, the grouping algorithm was re-applied, again creating objects with >15 voxels with connected faces that usually consisted of single beads then. Since single voxels in each object (or each oxygen sensor bead) contained low numbers of photons in their decay traces (typically 10-150 photons), decay traces from all voxels in each bead were grouped to retrieve one decay trace per bead. Beads with less than 1000 photons total were deleted to ensure sufficient photon number for data fitting with low errors. The corresponding analysis is presented below.

Since each detection unit of the single photon counting system had a specified dead-time of 100 ns after each registered photon event, the beginning of decay curves where intensities were still higher typically suffered from photon loss which skewed the consecutive fit and lead to a decrease in fitted lifetime with increasing intensity. Thus, the decay traces were corrected for detector saturation. The lowest change in oxygen tensions when recording samples with 10-fold increases in intensity were observed when using a dead time of t_d = 55 ns. The system contained 2 parallel detection units with a polarization splitter in the optical.

Then, decay traces for each bead were fitted and the retrieved lifetime parameter was translated into an oxygen tension through previously recorded calibration curves. The oxygen sensor beads

were then plotted in 3D at the center of the XY position of the 3D object and the Z-plane with the highest photon intensity. Live cell maps acquired in parallel were overlayed.

1.2 Time-dependent data from multiple voxels within a sensor bead can be summed

The acquired data consists of photon counts distributed in discrete time "bins" (256 in the setup used) after excitation of each voxel. As discussed in the main text, the number of photons arriving from a single voxel after a single excitation cycle is insufficient for high-quality curve fitting. Thus, the binned photon counts of multiple voxels within each bead should be summed by bin to provide better total counting statistics. This is only possible if all voxels of each bead do indeed have equivalent intensity decay profiles. We examined the degree of equivalence extensively within the spatial extent of each bead for multiple beads and for multiple dissolved oxygen concentrations. Formally, this is an assessment of whether the time-dependent photon count distribution from all bead voxels is drawn from the same Poisson distribution. Fig. S2 shows representative examples of the observed intensity profiles (blue bars) from 4 distinct voxels within one bead at dissolved oxygen concentrations of 20.9% (a) or 0% (b), each intensity distribution resulting from the summation of 20 repeated acquisitions at each voxel. The summed intensity distribution from each voxel was subsequently fitted by the decay profile found to be optimal (bi-exponential intensity decay with a predetermined background, see ESI section 1.4). The parameters of the fitted profile to each voxel's intensity decay curve are found to be statistically indistinguishable from the profile acquired at the other three voxel locations, at either oxygen concentration investigated. This supports the assumption of the time-dependent intensity distribution of different voxels within a bead being drawn from the same Poisson distribution, and that bin-wise summation of the photon count distributions of separate voxels is analytically valid.

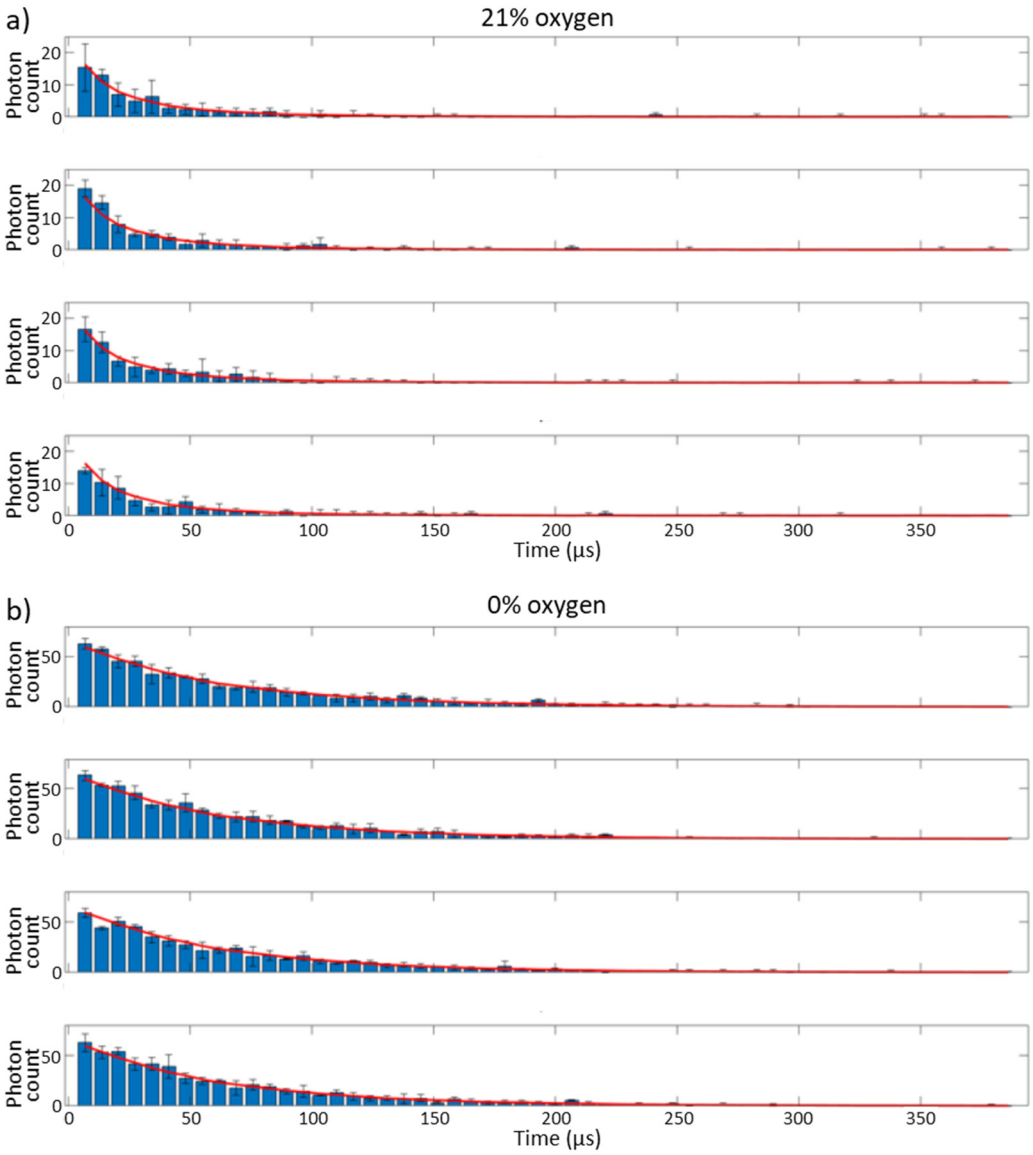

Fig. S2 The four graphs for each oxygen concentration show the recorded data (blue bars) with standard deviation error bars of the mean, and with the mean (red line) across all pixels belonging to that bead. The 4 randomly chosen pixels that are shown for each oxygen concentration illustrate that the data from each individual pixel seems to originate from the same distribution. The plots shown in this Fig. represents what was a general observation on multiple datasets. The data set was recorded by summing 20 image frames at the same imaging height.

1.3 Non-linear least squares fitting cannot capture the intensity distribution at low photon counts

Intensity decay profiles have most commonly been fitted using non-linear least squares fitting (NLLS) protocols that assume a normal distribution of data values. This is a good approximation for high photon counts, using extended acquisition times, where the underlying Poisson distribution becomes indistinguishable from the normal distribution. However, the approximation fails at the low photon counts resulting from the targeted fast mapping of a 3D volume. Fig. S3 compares three commonly used NLLS fitting functions for intensity decay, (*i*) a single exponential (red curve), (*ii*) a stretched exponential (green curve), and (*iii*) a biexponential with a predetermined background (purple curve), applied to data recorded on a sensor bead at 20.9% oxygen. The photon counts are presented on a logarithmic scale to highlight the low-intensity observations at longer decay times. The single exponential poorly fits the observations throughout the decay time. Both the stretched exponential and the biexponential fitted by NLLS follow the observations at high photon counts but fail to correctly describe the tail of the decay profile. In contrast, Maximum Likelihood Estimation (MLE) works for any type of statistical distribution including the Poisson distribution and with NLLS being the limiting case of MLE of a Poisson distribution for large numbers of observations. This is illustrated in Fig. S3, where MLE fitting of a biexponential with a predetermined background (see ESI section 1.4) captures the photon count distribution both in the beginning (high photon counts) and the end (low photon counts approaching the background level) of the recorded decay trace. Thus, MLE is the preferred method of fitting the observations and extracting effective lifetimes in the developed analysis protocol.

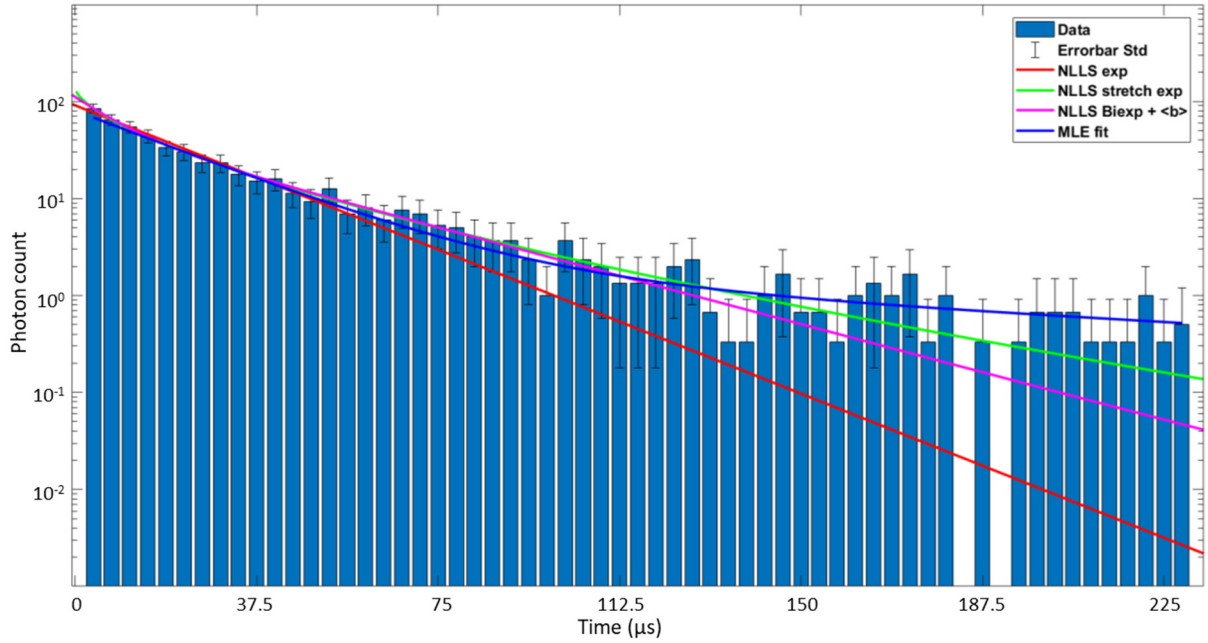

Fig. S3 Comparison of the most used NLLS-based fitting functions in single-photon counting applications and the best performing MLE function. The data originates from a sensor bead at 20.9% oxygen. The data has been re-binned from 182 to 61 bins for visualization. Each bar represents the mean of the original bins, and the error bars show the standard deviation of the mean. Comparing the NLLS and MLE bi-exponential fits show the impact of the distribution assumption being normal and Poisson, respectively.

1.4 Selection of fitting function by application of the AIC criterion and a derived scoring system

The Akaike information criterion (AIC) assesses the quality of a fit penalized by the number of free parameters in the fit. Calculated AIC values are smaller for a better fit and/or a smaller number of parameters, which is preferred. We calculated AIC values for each type of fitting function applied to acquired data for each bead at different oxygen concentrations to find the preferred function. The three tested functions are:

- Single exponential: $\langle n_i \rangle = \frac{\langle N \rangle}{\tau} \int_{(i-1)\Delta t}^{\Delta t} \exp(-t/\tau)\, dt, \;\; i = 1, \dots, N$
- Stretched exponential: $\langle n_i \rangle = \frac{\langle N \rangle\, \beta}{\tau\, \Gamma(\frac{1}{\beta})} \int_{(i-1)\Delta t}^{\Delta t} \exp\left(-[t/\tau]^{\beta}\right) dt, \;\; i = 1, \dots, N$
- Biexponential: $\langle n_i \rangle = \frac{\langle N \rangle}{a\tau_1 + (1-a)\tau_2} \int_{(i-1)\Delta t}^{\Delta t} [a \exp(-t/\tau_1) + (1-a) \exp(-t/\tau_2)] dt, \;\; i = 1, \dots, N$

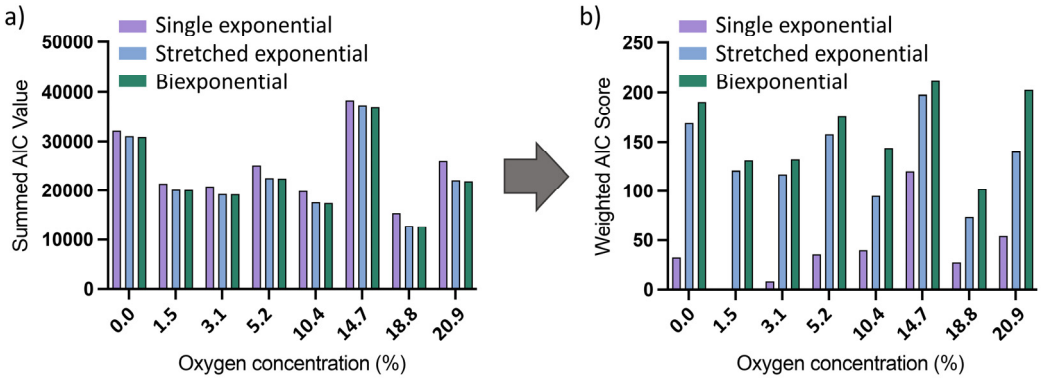

Fig. S4 Selection of fitting function by application AIC criterion and translation into AIC scoring system. (a) Summed AIC values of all beads in measurements at 0% to 20.9% oxygen for single, bi- and stretched exponential function and (b) corresponding weighted AIC score.

Fig. S4 shows the summed AIC values for calibration measurements from 0 % to 20.9 % O_2 for single exponential, bi-exponential and stretched exponential functions (Fig. S4a) and the corresponding weighted AIC score (Fig. S4b). As is apparent, the single exponential function had the highest summed AIC value (poorest fit), the stretched exponential the second highest and the bi-exponential function the lowest AIC value (best fit) across all oxygen tensions. The summed AIC value for each fitting function and oxygen tension is retrieved by summing the AIC values of all beads in a measurement. Strong outliers in AIC values from single beads in the bead population of a measurement and fitting function would not be apparent here and could distort the result. Thus, a weighted AIC score was calculated. The scoring system worked as follows: For each single oxygen sensor bead, a single, bi- and stretched exponential fit was applied and the AIC scores were compared. The function with the lowest resulting AIC each individual bead was scored with 3 points, the function with second lowest AIC value got scored with 2 points, and the one with the highest AIC value got 1 point. This way, the fitting function with low AIC values for most oxygen sensor beads could be identified. Fig. S4b confirms that the biexponential function not only has the lowest summed AIC values but also has the highest weighted AIC score across all oxygen tensions, followed by the stretched exponential and with significant gap the single exponential.

1.5 Influence of lower intensity cut-off on oxygen measurement accuracy

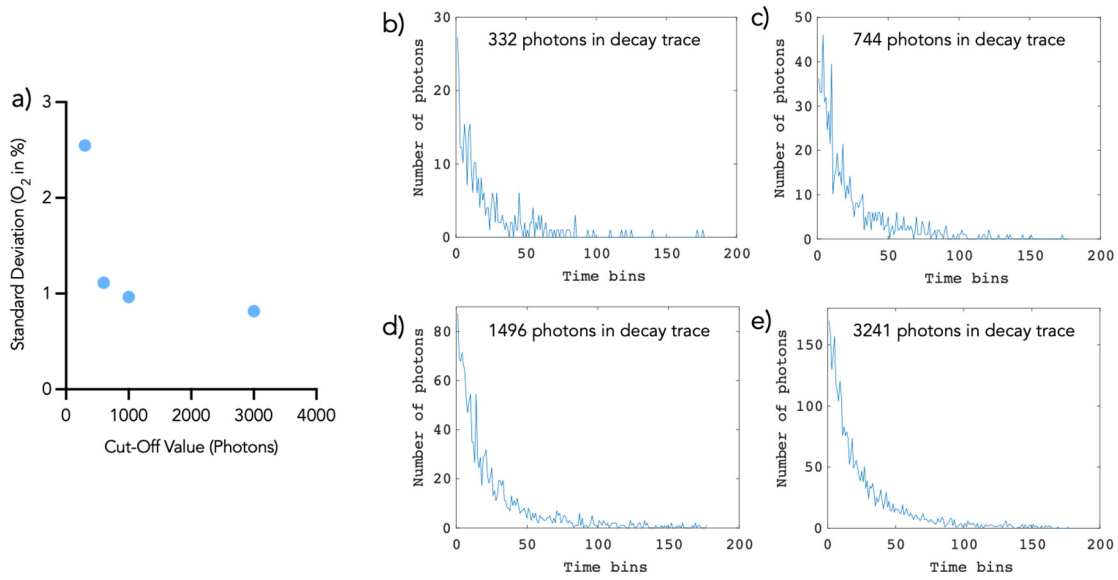

Fig. S5 The influence of cut-off values for minimum number of photons per oxygen sensor bead on standard deviations in calibration measurements. (a) Standard deviation in oxygen sensor bead population at different photon intensity cut-off values (minimum photon number per oxygen sensor bead). (b-e) Phosphorescence decay curves of oxygen sensor bead with lowest intensity in analysis with cut-off values of 300, 600, 1000 and 3000 photons. Calibration measurement at 10.5% O_2 used for comparative analysis.

Two major factors influencing oxygen measurement accuracy are (*i*) the number of photons per bead that influence the quality of fits to phosphorescence decay curves and (*ii*) the oxygen tension range of the measurement, since the relation between phosphorescence lifetime and oxygen tension is non-linear. High photon numbers lead to smoother decay curves and thus more accurate fits but are negatively correlated with imaging depth and speed. In addition, given the non-linear relation of phosphorescence lifetimes and oxygen tension, in measurements at low oxygen tensions, the error in oxygen tension due to fitting errors in lifetimes is smaller compared to measurements at high oxygen tensions.

Fig. S5 shows the influence of cut-off values for minimum number of photons per oxygen sensor beads on the standard deviation in calibration measurements. This is relevant when determining the required accuracy for an experiment at hand. It is apparent in Fig. S5 that standard deviations in oxygen measurements strongly decrease when increasing the photon cut-off for oxygen sensor beads from 300 to 600 photons, while flattening off towards photon cut-off values of 1000 and 3000 photons per bead. Fig. S5b-e show decay traces from beads with the lowest intensities in a measurement with cut-off values of 300, 600, 1000 and 3000, respectively, illustrating the underlying phosphorescence decay profiles used to extract phosphorescence lifetime. For typical measurements, a cut-off value of 1000 photons per bead was used in this work. However, depending on the oxygen tension range of interest and required accuracy, this can be increased or decreased.

1.6 Uncertainty of the oxygen concentration estimation

The phosphorescence lifetime is strongly dependent on oxygen concentration at low concentration, while the dependence is much weaker at ambient conditions. The standard deviation (s.d.) of the fitted lifetime using the chosen MLE biexponential fit procedure (ESI section 1.4) varies much less with oxygen concentration, as shown in Fig. S6. This implies that the absolute uncertainty on the estimated concentration is much lower at low oxygen concentrations (<10% DO_2), which is also the physiologically most relevant range. The predictive accuracy is estimated from a plot of the calibration curve offset vertically by positive and negative 2 s.d. to indicate the range where 95% of the observations are expected. Reading off the range of oxygen concentrations spanned by the two offset curves, the uncertainty is estimated to be <1% DO_2 for oxygen concentrations <5% DO_2, <3% DO_2 for oxygen concentrations <10% DO_2, and up to <5% DO_2 for oxygen concentrations >10% DO_2.

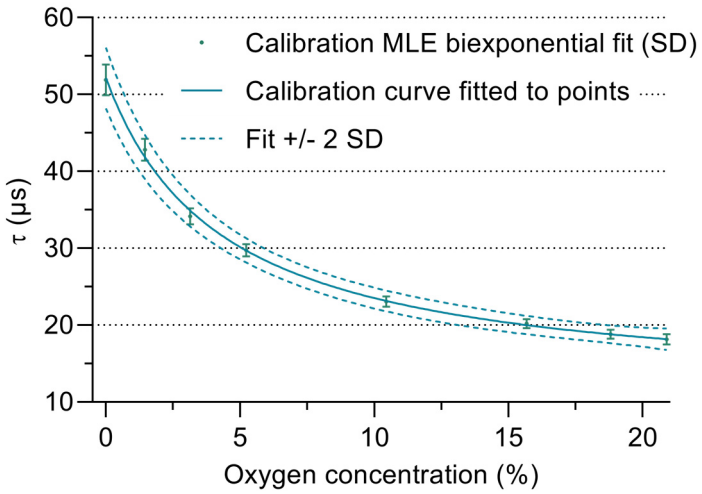

Fig. S6 Calibration curve (solid curve, same as in main text Fig. 4e) fitted to data points obtained from an MLE biexponential fit to the decay curves at selected defined oxygen concentrations. The error bars show the s.d. on the fitted decay time (not s.e.m). S.d.s at other oxygen concentrations are interpolated by fitting all the s.d. values from data points to a 4th order polynomial. The calibration curve is subsequently offset vertically (dashed lines) by -2 s.d. and +2 s.d., respectively, to illustrate the expected range of 95% of the measurements.

2 Vertical accuracy of the bead position analysis

The lateral position of each sensor bead can be determined with high accuracy, while the accuracy of its vertical position is limited by the numerical aperture of the objective and by the optical properties of the bead material. The apparent vertical extent can be assessed from analysis of a confocal stack of sensor beads embedded in a hydrogel at different heights. The presence of embedded cells might influence the optical quality, so the analysis was performed on a hemispherical droplet as also analyzed in the main text (Fig. 2). Fig. S7a shows overlaid fluorescence and phosphorescence, while Fig. S7b only shows the phosphorescence. The dashed line indicates the location for performing a vertical cross-section through a random bead shown in the insert below (labeled XZ). Fig. S7c is a zoom on the cross-sectional view of that bead, suggesting an apparent vertical extent of 200-300 µm and with a pronounced intensive maximum spanning approximately 100 µm.

Acquisition of each confocal stack uses a physical height difference of 20.0 µm. This corresponding optical path length difference between imaging planes is taken to be 26.6 µm, approximating the refractive index of the hydrogel surroundings by that of pure water ($n = 1.33$). The apparent vertical extent of 6 random beads is investigated quantitatively, with the selection criterion being that they have their maximum observed phosphorescence intensity at an image plane separated by 5 imaging planes from another bead. Fig. S7d presents the results of the analysis. The horizontal axis shows the depth (image plane) where each of the beads has the largest summed photon count, i.e., the bead center. The vertical axis shows the sampling depth range (image planes) for all 6 beads. Each horizontal bar in the violin plot represents the relative summed photon count in that image plane. The quantitative analysis suggests an extent of the intensity maximum of no more than 2 image planes, i.e., approximately 45 µm in vertical extent, and it is obvious that fitting of the summed counts from all vertical position allows for highly accurate prediction of the vertical intensity maximum.

Accurate placement of color-coded oxygen sensor depictions in 3D volumes was evaluated by overlaying XY and XZ phosphorescence maximum intensity projection images with oxygen sensor maps, shown in Fig. S7e+f. Both XY and Z oxygen sensor depictions are observed to be co-located with corresponding phosphorescent signal from the original oxygen sensor beads in the sample volume.

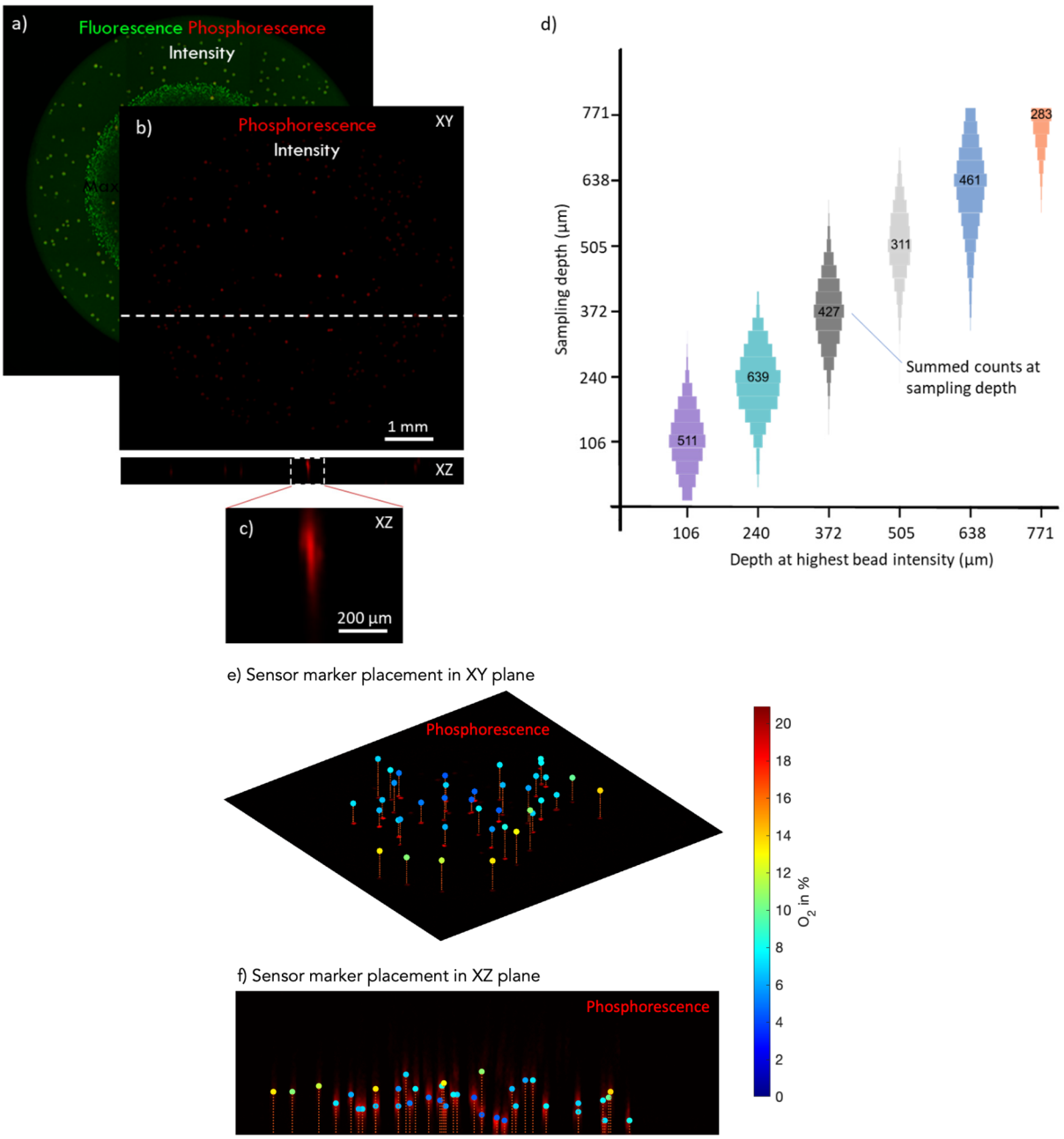

Fig. S7 Analysis of the apparent vertical extent of sensor beads. (a) Overlaid maximum projections of fluorescence and phosphorescence from a hemispherical GelMA hydrogel with embedded sensors beads (green and red) and live-stained cells (green). (b) A single image plane (XY) of the underlying confocal stack showing only phosphorescence from the sensor beads. The dashed line indicates where the cross-sectional plane at the bottom (XZ) is extracted. (c) Five times magnification of the outlined part of the XZ cross-section, showing the vertical and lateral extent of a single sensor bead as observed in the confocal stack. (d) Vertical intensity distribution (summed photon counts) of 6 beads having their highest photon counts at different depths (horizontal axis). The width of each level of the violin plot of each bead shows its relative summed photon counts for varying imaging depths (shown on the vertical axis), with the summed photon count at the plane of its highest photon count specified. (e, f) Maximum intensity projections of 3D phosphorescence intensity image with 256x256x50 voxels (50 z-planes recorded with 20 µm stepping) along with oxygen sensor placement. Location on XY plane indicated with red dots below color-coded oxygen sensor depictions.

3 Numerical modeling of oxygen distribution profiles in 2D cultures

Oxygen diffusion in 96 well plates with 2D cultures of Hep G2 cells covered with medium of different heights, matching the experimental conditions analyzed in Fig. 5, was numerically modeled using COMSOL 5.5 (COMSOL AB). The confluency of the Hep G2 cell layer was visually estimated to be 80% corresponding to a cell density of approximately $80 \cdot 10^3$ cells/cm^2 for all three culture conditions, i.e., medium heights of 1.5 mm (50 µL), 3.0 mm (100 µL), or 6.0 mm (200 µL). The oxygen consumption rate was modeled by a Michael-Menten dependence with a Michaelis constant $K_M = 4\ \mu\text{M}$ and a maximum consumption rate of $v_{max} = 1.1 \cdot 10^{-16}\ \text{mol cell}^{-1}\ \text{s}^{-1}$. The oxygen diffusion constant was set to $D_{O2} = 3.2\ \times 10^{-9}\ \text{m}^2\text{s}^{-1}$ in water at 37 °C,[1] and a boundary condition of constant dissolved oxygen concentration at the medium/air interface of $c(O_2) = 177\ \mu\text{M}$ (corresponding to 18.7% O_2 in a 95% air / 5% CO_2 / 100% relative humidity gas mixture at at 37 °C) [2] was applied. The results are displayed in Fig. S8, showing good agreement with the experimentally observed oxygen concentrations at the level of the cell layer in Fig. 5.

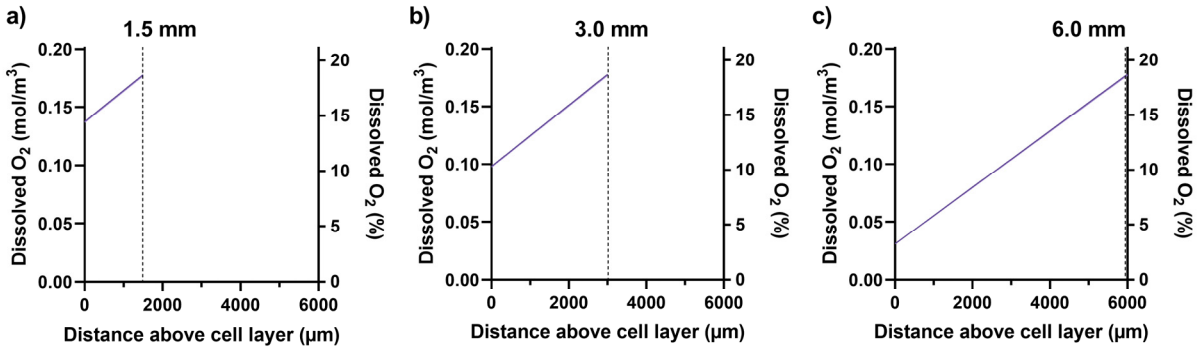

Fig. S8 Numerical simulation of dissolved oxygen concentration profiles above a 2D cell layer for medium heights of (a) 1.5 mm, (b) 3.0 mm, and (c) 6.0 mm.

4 From 3D CAD models to oxygen distribution profiles

The microfluidic chips were designed in Inventor 2018 (Autodesk). The chip designs included flow distribution volumes at the entry to and exit from the microfluidic channel(s) of the 1-channel or 8-channel systems, as well as cylindrical holes (inner diameter 0.70 mm) at the chip inlet and outlet to enable stable fluidic connection to an external fluidic pump by insertion of slightly larger (outer diameter 0.80 mm) blunted hypodermic needles (Fig. S9a Cross-Section).

Oxygen transport within the cell culture volume was numerically modeled using COMSOL 5.5 (COMSOL AB). Cross-sections of the two modeled geometries, matching the design channel dimensions of the physical chip, are shown in Fig. S9b, and the cross-sections were axially extruded to the length of the designed channels within the confines of the cell culture volume. Oxygen is transported into the model by convective flow (specified average flow rate) with an entry boundary condition of the equilibrium concentration for oxygen in water at 37 °C (ambient of 95% air/5% CO_2, ionic strength of 170 mM).[2] The oxygen diffusion rate in all modeled volumes (medium, channel wall, culture volume) is approximated with the value of oxygen diffusion in pure water at 37 °C. Oxygen consumption in the cell culture volume is modeled by a Michaelis-Menten model using a Michaelis constant $K_M = 4\ \mu\mathrm{M}$ [3] and varying $V_{\max}$ to match the observed oxygen distribution. The cell densities were estimated from the known doubling time of the Hep G2 cells [4] and a culture time of 3 days in the chips.

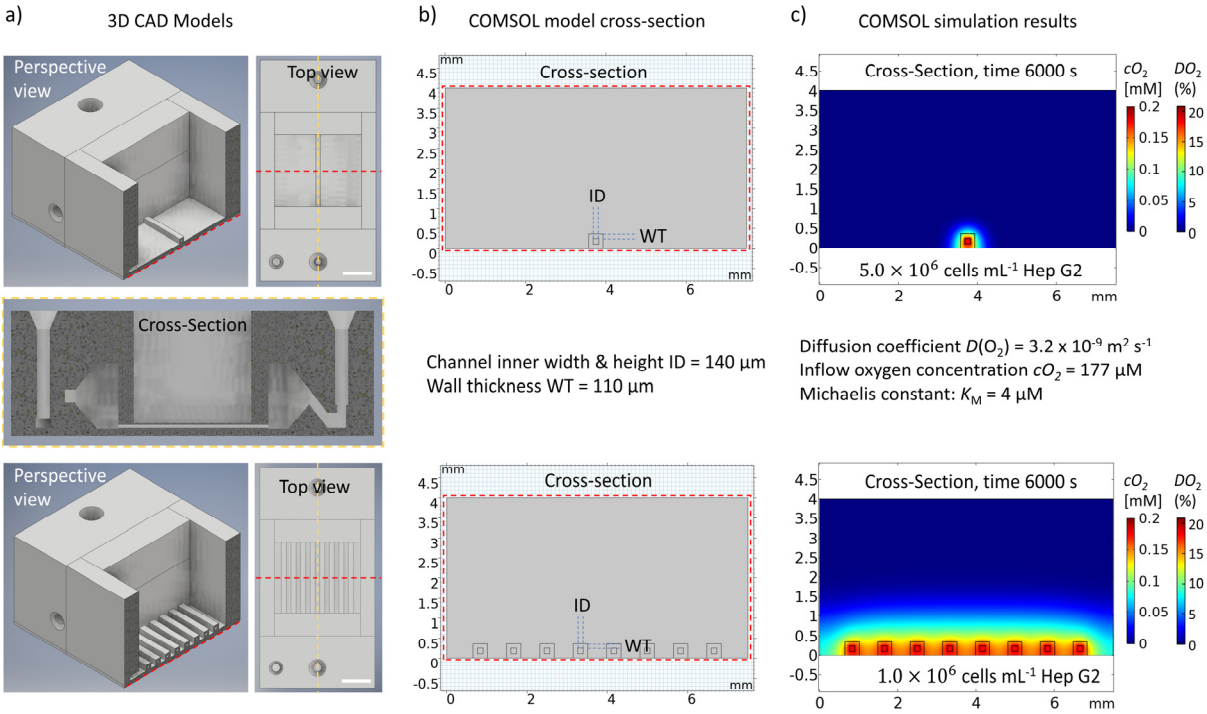

Fig. S9 Simulation of medium perfusion, oxygen diffusion and cellular oxygen consumption in microperfused cell culture scaffolds. In (**a**) 3D CAD models of 1-channel and 8-channel synthetic vasculature chips in areal; top and cross-sectional views are depicted. In (**b**) simplified 2D COMSOL models of cross-section through 3D CAD models (red dashed line) shown. In (**c**), simulation of oxygen distribution in 1-channel and 8-channel models with perfusion, oxygen diffusion and cellular oxygen consumption are shown. Scale bar (a, top view) 2.5 mm.

5 Comparison of flow velocity-dependent oxygen gradients in simulations and measurements

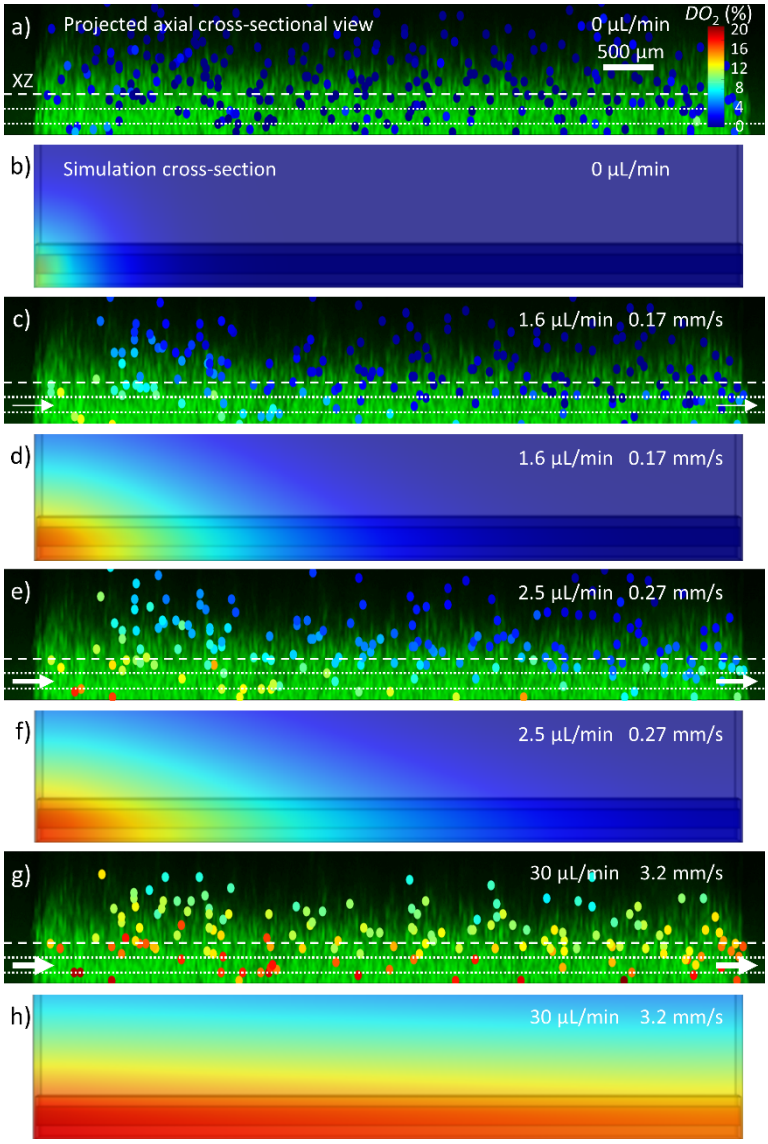

Fig. S10 Comparison of measured and numerically modeled axial oxygen concentration profiles for different perfusion rates in the 8-channel chip design at average channel flow velocities of (a and b) 0 mm/s, (c and d) 0.17 mm/s, (e and f) 0.27 mm/s, and (g and h) 3.2 mm/s. The experimental and numerically simulated seeding density is 2×10^6 cells/mL at all flow conditions.

References for Electronic Supplementary Information

1 E. O. Pettersen, L. H. Larsen, N. B. Ramsing and P. Ebbesen, *Cell Prolif.*, 2005, **38**, 257–267.

2 B. A. Wagner, S. Venkataraman and G. R. Buettner, *Free Radic. Biol. Med.*, 2011, **51**, 700–712.

3 C. Magliaro, G. Mattei, F. Iacoangeli, A. Corti, V. Piemonte and A. Ahluwalia, *Front. Bioeng. Biotechnol.*, 2019, **7**, 1–9.

4 E. E. Furth, H. Sprecher, E. A. Fisher, H. D. Fleishman and M. Laposata, *J. Lipid Res.*, 1992, **33**, 1719–1726.